Hot Plasma and Black Hole Binaries in Starburst Galaxy M82

R. E. Griffiths,[1]* A. Ptak,[1] E. D. Feigelson,[2] G. Garmire,[2] L. Townsley,[2] W. N. Brandt,[2] R. Sambruna,[2] J. N. Bregman[3]

High-resolution x-ray observations of the prototype starburst galaxy Messier 82 (M82) obtained with the advanced CCD (charge-coupled device) imaging spectrometer on board the Chandra X-ray Observatory provide a detailed view of hot plasma and energetic processes. Plasma with temperature of about 40,000,000 kelvin fills the inner 1 kiloparsec, which is much hotter than the 1,000,000 to 2,000,000 kelvin interstellar medium component in the Milky Way Galaxy. Produced by many supernova explosions, this central region is overpressurized and drives M82's prominent galactic wind into the intergalactic medium. We also resolved about 20 compact x-ray sources, many of which could be high-mass x-ray binary star systems containing black holes.

A starburst galaxy is one undergoing a violent and unsustainable burst of star-forming activity, evidenced by excesses of infrared, radio, and x-ray emissions produced by the massive stars, supernovae, and heated interstellar dust (*1*). Starburst galaxies are often triggered by close encounters between two galaxies and may have been prevalent in the early universe. Characterization of starburst galaxy processes is seminal to our understanding of galaxy formation in the early universe, galaxy interactions and mergers, and the chemical enrichment of the interstellar medium within galaxies and the intergalactic medium between galaxies (*2–5*). Although the formation of the first generation of stars and galaxies in the universe is difficult to study at cosmological distances, starburst processes can be examined in detail in nearby prototype starburst galaxies. X radiation is particularly valuable for revealing the products of copious and rapid star formation: the hot component of the interstellar medium produced by supernova remnants, accretion-driven x-ray binary star systems, and possibly a nascent active galactic nucleus powered by a massive black hole (MBH).

Messier 82 [M82 = New General Catalog (NGC) 3034], at a distance of 3.6 Mpc (*6*), just outside the Local Group of galaxies, is the closest galaxy with a far-infrared (FIR) luminosity that exceeds the luminosity at visual wavelengths ($L_{FIR} > L_V$). Its inner ≃500 pc is experiencing a violent episode of star formation following a close encounter with the neighboring galaxy, M81, about 100 million years ago. Though intrinsically a relatively small galaxy with an optical extent of 12 kpc and a dynamical mass of $\simeq 1.5 \times 10^{10}$ $M_\odot$ (where $M_\odot$ is solar mass), for the past 5 to 50 million years, it has been converting ~10 $M_\odot$/year into stars with a phenomenal supernova rate of ~0.1 supernovae per year (*7*).

Following initial detection as an x-ray source (*8*), M82 has been extensively observed with the Einstein, ROSAT (Röntgen Satellit), and ASCA (Advanced Satellite for Cosmological Astrophysics) orbiting x-ray observatories [e.g., (*9–14*)]. The total x-ray emission varies from $L_x \simeq 3 \times 10^{40}$ to 10×10^{40} erg s^{-2} (0.5- to 10-keV band). An x-ray–emitting wind extending tens of kpc perpendicular to the disk is generated by the starburst. However, past x-ray observations have been difficult to interpret because of limited combinations of spatial and spectral resolution. For example, it has not been clear as to how much of the baseline steady state flux is due to processes in diffuse systems or to the combined emission from many stellar sources, whether the diffuse emission is thermal or nonthermal in origin, or whether the highly variable harder emission arises from a central MBH or an x-ray binary system.

The advanced CCD (charge-coupled device) imaging spectrometer (ACIS) on the Chandra X-ray Observatory (CXO) (*15–17*) can be used to resolve these complex structures in nearby starburst galaxies. We observed galaxy M82 with the four-CCD ACIS-I array for 35 ks on 20 September 1999. After reduction of the data and adaptive smoothing, the central region of M82 (800 pc by 800 pc) shows compact and diffuse structures in the soft (0.5 to 2.0 keV) and hard (2 to 10 keV) x-ray bands (Fig. 1) (*18*).

The total brightness of M82 was unusually low during the ACIS observation. For an absorbed power law spectrum with energy index $\alpha = 0.8$ and hydrogen column density $N_H = 1.0 \times 10^{21}$ cm^{-2} (*12*), the ACIS hard (2 to 10 keV) flux is 1.0×10^{-11} erg s^{-1} cm^{-2}, and for an absorbed plasma model with temperature $T = 10^7$ K and $N_H = 0.5 \times 10^{21}$ cm^{-2}, the soft (0.5 to 2.0 keV) flux is also 1.0×10^{-11} erg s^{-1} cm^{-2}. The soft flux, which is not expected to vary, is consistent with ASCA measurements, whereas the hard flux is as much as a factor of 5 lower than the peak ASCA measurement and 30% lower than the lowest historical ASCA flux (*14*). The low value of the hard flux can only be accounted for by variability of one or more sources. The large variation in the hard x-ray

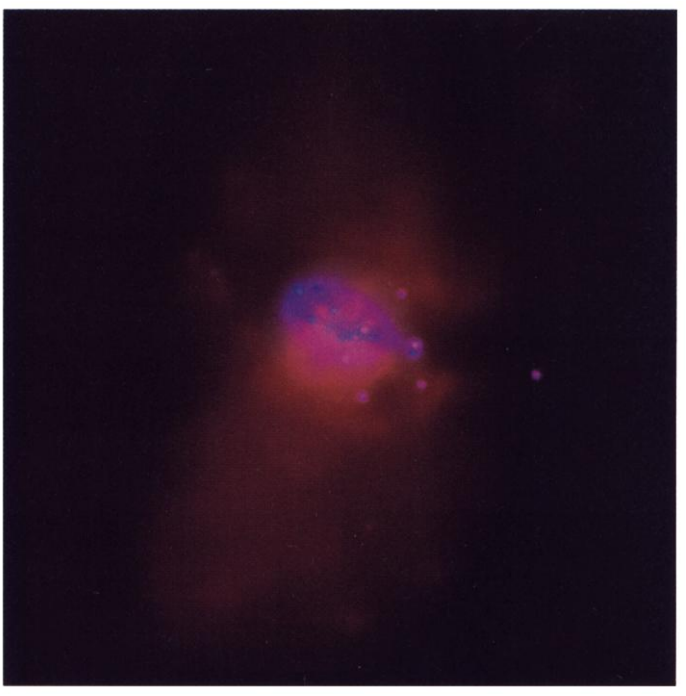

Fig. 1. The central region of the galaxy in soft (0.5 to 2.0 keV, in red) and hard (2 to 10 keV, in blue) x-ray bands after reduction of the data and adaptive smoothing to reveal compact and diffuse structures simultaneously (*18*). North is up and east is to the left. The overall width of the image is ~4 kpc.

[1]Department of Physics, Wean Hall, Carnegie Mellon University, Pittsburgh, PA 15213–3890, USA. [2]Department of Astronomy and Astrophysics, 525 Davey Laboratory, Pennsylvania State University, University Park, PA 16802, USA. [3]Astronomy Department, Dennison Building, University of Michigan, Ann Arbor, MI 48109, USA.

*To whom correspondence should be addressed. E-mail: griffith@astro.phys.cmu.edu

emission suggests that a large fraction of this emission arises from a small number of compact highly variable sources. The ACIS observations show that ~60 to 75% of the 2- to 10-keV flux is resolved into point sources (Fig. 2, C and D).

To a flux limit of 10^{-15} erg cm^{-2} s^{-1} (2 to 10 keV), M82 contains 22 unresolved sources (diameter of <1″, or <170 pc) with L (2 to 10 keV) ~ 1×10^{37} to 10^{39} erg s^{-1}, all contained within the central region measuring 2.5 kpc by 2.5 kpc. About 30 other sources are present in the ACIS field farther from the center of M82. Most are probably background sources comprising distant active galactic nuclei and are used for astrometric alignment of the field (*18*). The fitted positions, hardness ratios (HRs), 2- to 10-keV fluxes, and luminosities (assuming $N_H = 1 \times 10^{21}$ cm^{-2} and $\alpha = 0.8$) are given in Table 1, where the HR is evaluated as $(H - S)/(H + S)$, where H and S are the 2.0- to 8.0-keV and 0.5- to 2.0-keV count rates, respectively. Previous observations with the ROSAT high-resolution imager (HRI) had been used to separate three point sources in the nuclear region (*10, 13*), but these sources were apparently "confused"; that is, the sources that were "resolved" by the HRI actually consisted of two or more of the sources in Table 1, with the exception of the brightest source, which is historically variable (*19*).

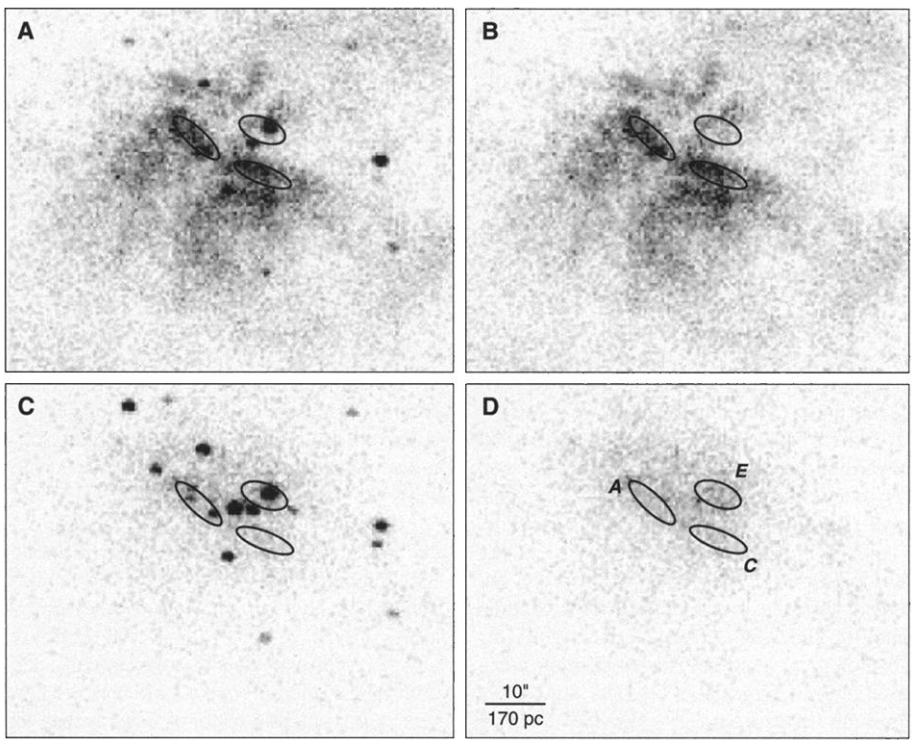

Fig. 2. The ACIS-I 0.5- to 2.0- and 2.0- to 8.0-keV maps, with and without point sources. (**A**) The 0.5- to 2.0-keV image, including point sources. (**B**) The 0.5- to 2.0-keV image, with point sources removed. (**C**) The 2.0- to 8.0-keV image, including point sources. (**D**) The 2.0- to 8.0-keV image, with point sources removed. Regions corresponding to super star clusters A, C, and E of (*31*) are marked with ellipses and labeled in (D).

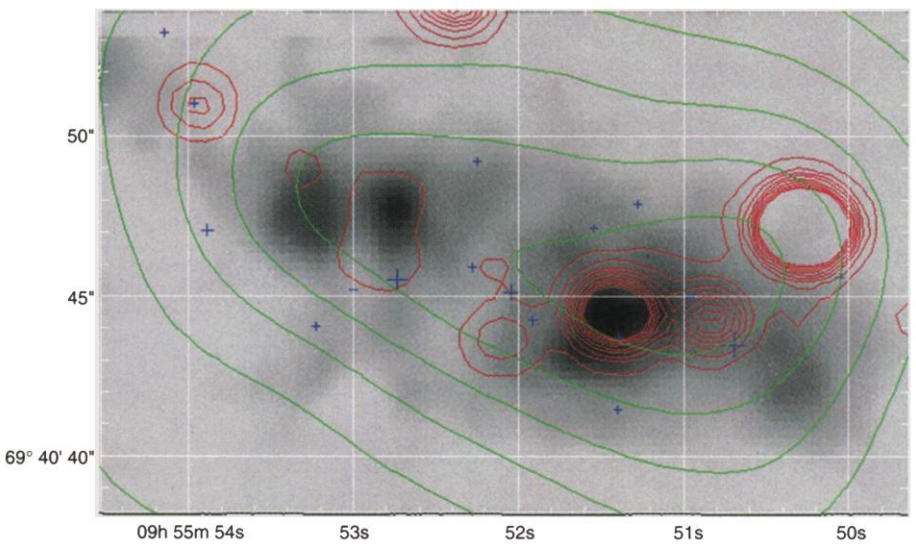

Fig. 3. The gray-scale image was created with the mid-infrared intensity image (*32*). The red contours are from the hard 2- to 8-keV image after smoothing with a 0.5″ Gaussian (contours are linear at intervals of two smoothed counts per pixel), and the green contours are from the same hard x-ray image after subtracting sources and smoothing with a 1″ Gaussian (contour levels are 0.5 smoothed counts per pixel). The blue crosses are radio sources (*33*), and the brighter sources are shown with larger crosses.

The source that has been historically brightest, CXOM82 095550.3+694046, is seen here reduced in strength by a factor of ~10, compared with the peak ASCA flux (*10, 11, 14, 19*). This source is 10″, or 0.16 kpc, from the centroid of infrared and radio emission, which may also be the dynamical center of the galaxy at the coordinate position right ascension $09^h55^m52^s.4+69°40'46''$ (J2000) (*20*). The variability has been used to argue that this source is a nascent MBH with a mass of ~400 to 500 $M_\odot$, intermediate between the masses of black holes in binary star systems and those commonly found in massive galaxies (*14*). At least six of the other ACIS sources (Table 1) with $L_x \geq 3 \times 10^{38}$ erg s^{-1} may be x-ray binary systems with emissions exceeding the Eddington limit of neutron stars. The compact accreting objects in these binary systems are probably black holes arising from the supernovae explosions of very massive "O" or Wolf-Rayet stars. Their hard spectra (HR ≥ 0.0) and high hard band luminosities are signatures of black hole binaries (*21*).

There is little overlap between the x-ray source positions and radio-detected young supernovae remnants (SNRs) (Fig. 3); therefore, our results do not support the previous claims (*13*) that the compact x-ray sources in M82 are predominantly SNRs. Only one ACIS source, CXOM82 095554.0+694050, lies within 1.0″ of a radio SNR. The radio source 44.01+59.6, suggested to be an active galactic nucleus (*22*), does not have a compact x-ray counterpart, although the eighth brightest source CXOM82 095552.9+694046 [with L (2 to 10 keV) = 1.7×10^{38} erg s^{-1}] lies 1.1″ away and cannot be ruled out.

One of the hallmarks of the starburst nature of M82 is the number and high luminosity of its OB associations, often called "super" star clusters. A few of the less obscured super star clusters, M82A through M82F, have been imaged with the Hubble Space Telescope (*23*). Much of the soft central x-ray emission appears to be associated with these

unobscured super star clusters (Fig. 2B and Table 1), which may also be responsible for a few of the hard x-ray sources that appear to be resolved at a scale of $\sim 1'' \simeq 12''$. There is also an association between the brighter mid-infrared (12 μm) intensity peaks from embedded super star clusters and concentrations of x-ray flux (Fig. 3). Integrated over its 3″ by 10″ extent, the L_x of the brightest super star cluster M82A with optical luminosity $L_V \simeq 10^{42}$ erg s^{-1} is $\simeq 1.6 \times 10^{38}$ erg s^{-1} and $\simeq 6.0 \times 10^{38}$ erg s^{-1} in the soft and hard bands, respectively. By analogy with the star-forming region 30 Doradus in the Large Magellanic Cloud (*24*), this x-ray emission could plausibly arise either from the diffuse plasma produced by many merged SNRs, the collective emission from many unresolved compact x-ray binary systems, or the hot winds of young massive stars. The typical x-ray emission from a young massive O star is 5×10^{33} erg s^{-1}, so that 10^5 such stars would be needed to account for the extended emission in the super star clusters. Such a number is consistent with estimates based on optical and ultraviolet studies (*23*).

Turning now to the diffuse emission, we find that its spatial distribution in the hard band (Fig. 3) can be modeled (*25*) as an elliptical exponential distribution, with the radii of the minor and major axes measured at 5.4″ (5.2″ to 5.5″) and 7.2″ (6.9″ to 7.4″) and an angle of 17° ± 4°, consistent with the position angle of M82 of 21° (i.e., the hard diffuse emission is aligned with M82's galactic disk). This model is preferred to an elliptical Gaussian model or a filled ellipsoid model {emissivity ∝ $[1 - (x/\sigma_x)^2 - (y/\sigma_y)^2]^{1/2}$}. The intensity of this emission does not increase in proximity to the point sources, indicating that it is not due to scattering by the telescope optics. The spectrum of the extended emission was extracted from a 50″ by 50″ (0.8 kpc by 0.8 kpc) region, with emission from point sources omitted and background from the opposite end of the imaging detector array subtracted (Fig. 3). The contributions of unresolved x-ray binaries [with luminosities less than L (2 to 10 keV) $\sim 10^{37}$ erg s^{-1}] are likely to be relatively unimportant, by comparison with the bifurcated luminosity function of x-ray binaries in the Magellanic Clouds for example (*26, 27*). The spectrum in the hard 2- to 10-keV band can be modeled by a power law with spectral index $\Gamma \simeq 2.5$ to 3.8, an absorbing column density $N_H < 1.0 \times 10^{21}$ cm^{-2}, and an iron emission line around $E \simeq 5.9$ to 6.9 keV with an equivalent width (EW) of 0.5 (0.1 to 1.9) keV ($\chi^2 = 89$, with 78 degrees of freedom; 90% parameter confidence levels) (*28*). The resulting integrated luminosity is $\sim L_x \simeq 2.2 \times 10^{39}$ erg s^{-1} in the hard band. In the soft band (Fig. 2B), the morphology and spectrum of the extended emission are complex and are not analyzed here in detail, except for the noted association with superclusters.

It has been proposed that the hard x-ray component in M82 is possibly nonthermal, resulting from inverse Compton scattering of infrared photons by the relativistic electrons that produce the large-scale radio emission (*12, 20*). We observed that there is indeed a diffuse component to the hard flux and that it constitutes ~30% of the hard band emission in the galaxy core (800 pc by 800 pc). In contrast to the predictions of nonthermal emission, however, we find that a substantial iron emission line is present, implying that some or all of the diffuse emission is thermal in origin. If the spectrum (Fig. 4) is due to a uniform hot thermal plasma, the plasma temperature is $kT \simeq 2.4$ to 4.1 keV (k, Boltzmann constant) and the iron line strength (EW, 0.5 keV) corresponds to an abundance of ~0.3 times the solar iron abun-

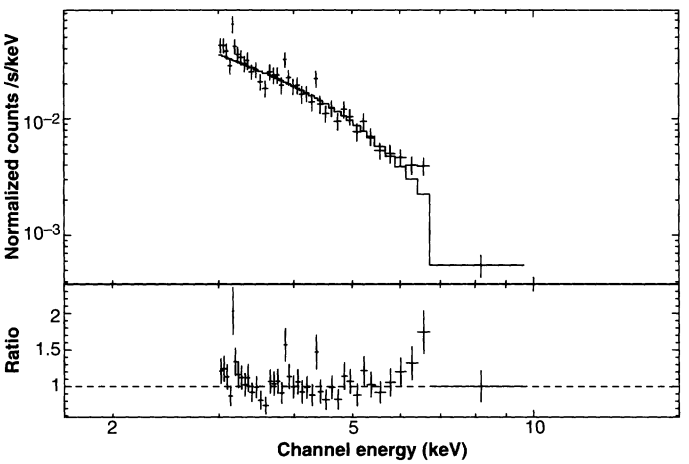

Fig. 4. The 3- to 10-keV ACIS-I spectrum of the diffuse central emission in M82. (Top) The data and the best fitting power law model spectrum. (Bottom) The ratio of data to model. The excess residuals around 6 to 7 keV are most likely due to Fe K emission.

Table 1. The individual compact x-ray sources within galaxy M82. HR is defined in the text. Fluxes (F) are in units of 10^{-12} erg cm^{-2} s^{-1} and luminosities (L) are in units of 10^{39} erg s^{-1}, derived from the 2- to 10-keV count rate assuming a power law spectrum with a slope of 0.8 and an absorption of $N_H = 10^{21}$ cm^{-2}. Counterparts in the final column include star clusters M82A, M82C, and M82E (*31*); near-infrared (NIR) star clusters (*34*); radio SNRs (*35*); and compact Hα sources (*36*), with offsets listed in parentheses.

Identification	HR	$F_{2.0-10.0\ keV}$	$L_{2.0-10.0\ keV}$	Counterparts
CXOM82 095538.3+694030	−0.40	0.0206	0.032	—
CXOM82 095544.5+693958	0.43	0.00256	0.00397	—
CXOM82 095546.4+694026	−0.21	0.0318	0.0492	—
CXOM82 095546.8+694041	−0.31	0.253	0.392	—
CXOM82 095546.9+694038	0.41	0.0616	0.0954	—
CXOM82 095547.7+694100	−0.16	0.0403	0.0625	—
CXOM82 095549.7+694043	1.00	0.0488	0.0757	M82E (5.5″)
CXOM82 095550.3+694046	0.42	1.9	2.94	M82 X-1 (0.7″), 41.30+59.6 (1.9″), M82E (1.3″)
CXOM82 095550.5+694022	−0.02	0.0455	0.0705	
CXOM82 095550.9+694044	0.44	0.303	0.469	41.95+57.5 (1.2″), 42.21+59.0 (0.9″), M82C (5.2″), M82E (2.9″)
CXOM82 095551.4+694043	0.99	0.907	1.41	NIR-9 (1.0″), NIR-10 (1.7″), NIR-11 (0.6″), NIR-12 (1.5″), 42.65+57.8 (0.7″), M82E (5.2″)
CXOM82 095551.7+694036	−0.02	0.164	0.255	—
CXOM82 095552.3+694043	0.23	0.113	0.175	NIR-5 (0.2″), 43.18+58.3 (1.4″), 43.31+59.2 (1.8″), M82A (3.3″)
CXOM82 095552.4+694054	0.63	0.399	0.618	—
CXOM82 095552.8+694046	−0.37	0.0349	0.054	NIR-1 (1.3″), NIR-2 (0.2″), M82A (2.7″)
CXOM82 095552.8+694047	0.81	0.107	0.165	NIR-2 (1.5″), 44.01+59.6 (1.1″), 44.28+59.3 (1.2″), M82A (1.6″)
CXOM82 095553.4+694047	−0.36	0.077	0.119	M82A (5.1″)
CXOM82 095553.6+693955	−0.18	0.011	0.017	—
CXOM82 095553.6+694102	0.59	0.0334	0.0518	—
CXOM82 095554.2+694050	0.98	0.145	0.225	45.24+65.2 (0.3″)
CXOM82 095554.8+694101	0.69	0.195	0.302	—
CXOM82 095601.1+694108	0.30	0.00959	0.0149	Hα-29 (0.2″)

dance. But, if we assume that the true iron abundance of the hot interstellar medium is solar, then we might be forced to infer that only 30% of the diffuse emission is actually thermal. Despite the observation of thermal line emission, it is thus difficult to rule out a component of diffuse emission from inverse Compton scattering. Assuming that the hard diffuse emission contains a major component of thermal origin (30 to 100% of the total) and integrating over the Gaussian elliptical region, we estimate that the plasma has a temperature of $\sim T \simeq 40$ MK and pressure of the order of $P/k \simeq 10^9$ cm^{-3}.

It seems quite likely that the hot component is not in hydrostatic equilibrium and is the basic driving force for the galactic wind outflowing perpendicular to the plane of M82. This hot x-ray–emitting gas is thus overpressurized as compared to the galaxy's gravitational potential well and is thus probably the principal driving mechanism for the hot outflow of chemically enriched material into the intergalactic medium. Such high-temperature plasmas in the cores of starburst galaxies may be the basic drivers for the chemical enrichment of the intergalactic medium and the intracluster medium within clusters of galaxies.

References and Notes

1. D. W. Weedman *et al.*, *Astrophys. J.* **248**, 105 (1981).
2. Y. Sofue, Ed., *The Central Regions of the Galaxy and Galaxies*, *IAU Symp. 184* (Kluwer, Dordrecht, Netherlands, 1998).
3. K. A. Van der Hucht, G. Koenigsberger, P. R. Eenens, Eds., *Wolf-Rayet Phenomena in Massive Stars and Starburst Galaxies*, *IAU Symp. 193* (Astronomical Society of the Pacific, San Francisco, 1999).
4. J. E. Barnes, D. B. Sanders, Eds., *Galaxy Interactions at Low and High Redshift*, *IAU Symp. 196* (Kluwer, Dordrecht, Netherlands, 1999).
5. S. Holt, E. Smith, Eds., *After the Dark Ages: When Galaxies Were Young* (AIP Press, New York, 1999).
6. W. Freedman *et al. Astrophys. J.* **427**, 628 (1994).
7. P. Kronberg, in *Galactic and Extragalactic Star Formation*, R. E. Pudritz, M. Fich, Eds. (Reidel, Boston, 1988), pp. 391–399.
8. R. E. Griffiths, M. D. Johnson, D. A. Schwartz, J. Schwarz, J. C. Blades, *Astrophys. J.* **230**, L21 (1979).
9. M. G. Watson, V. Stanger, R. E. Griffiths, *Astrophys. J.* **286**, 144 (1984).
10. J. N. Bregman, E. Schulman, K. Komisaka, *Astrophys. J.* **439**, 155 (1995).
11. T. G. Tsuru, H. Awaki, K. Koyama, A. Ptak, *Publ. Astron. Soc. Jpn.* **49**, 619 (1997).
12. E. C. Moran, M. D. Lehnert, *Astrophys. J.* **478**, 172 (1997).
13. I. R. Stevens, D. K. Strickland, K. A. Wills, *Mon. Not. R. Astron. Soc.* **308**, 123 (1999).
14. A. Ptak, R. E. Griffiths, *Astrophys. J.* **517**, L85 (1999).
15. M. C. Weisskopf, S. L. O'dell, L. P. van Speybroeck, *Proc. SPIE* **2805**, 2 (1996).
16. G. Garmire *et al.*, in preparation.
17. ACIS on the CXO provides sub–arc second imaging across a wide spectral band, low instrumental background rates permitting study of extended structures, and moderate spectral resolution at every pixel for astrophysical modeling.
18. The displayed images required several steps of data processing. With level 1–processed detected "event" lists, several types of events that were probably dominated by cosmic ray primary and secondary particles rather than imaged x-rays were removed: (i) event energies above 8 keV and below 0.2 keV; (ii) events split between pixels, except for standard ASCA grades; (iii) "hot columns" and other low-quality events; and (iv) brief periods of high background. The ACIS-I chips suffered radiation damage early in the Chandra mission, producing an increase in its charge-transfer inefficiency (CTI) during readout. To compensate for this effect, we recalibrated the ADU (analog-to-digital unit)-to-energy conversion for each photon as a function of its CCD pixel coordinate in the *y* direction (CHIPY) location using the calibration data set acisf1310. This correction is similar to that in (*29*) and produces individual photon energies accurate to ~10%. Our analysis here concentrates on events extracted from CHIPY > 700 in CCD I3, where most of the events detected from M82 are found. The resulting count-rate map was subject to adaptive kernel smoothing, which permits simultaneous viewing of compact and extended structures (*29*). Point sources were located with a multiscale wavelet analysis of the image (*30*). Although this procedure reliably detects isolated sources down to about seven photons, its sensitivity within the bright diffuse emission pervading the core of M82 is lower and difficult to determine quantitatively.
19. A. Collura, F. Reale, E. Schulman, J. N. Bregman, *Astrophys. J.* **420**, L63 (1994).
20. G. H. Rieke, M. J. Lebovsky, R. I. Thompson, F. J. Low, A. T. Tokunaga, *Astrophys. J.* **238**, 24 (1980).
21. D. Barret, J. E. McClintock, J. E. Grindlay, *Astrophys. J.* **473**, 963 (1996).
22. K. A. Wills, A. Pedlar, T. W. B. Muxlow, I. R. Stevens, *New Astron. Rev.* **43**, 633 (1999).
23. R. W. O'Connell, J. S. Gallagher, D. A. Hunter, W. N. Colley, *Astrophys. J.* **446**, L10 (1995).
24. L. Townsley *et al.*, in preparation.
25. These fits were performed with XIMGFIT, which is available at http://snooker.phys.cmu.edu/ximgfit. Photons from the sources in Table 1 were removed by replacing pixels where the contrast between the source model (Gaussian) and background model exceeded 50% by a Poisson deviate with a mean value given by the background model at that position.
26. H. V. D. Bradt, J. E. McClintock, *Annu. Rev. Astron. Astrophys.* **21**, 13 (1983).
27. A. P. Cowley *et al.*, in *The Stellar Content of Local Group Galaxies*, *IAU Symp. 192*, P. A. Whitelock, R. D. Cannon, Eds. (Astronomical Society of the Pacific, San Francisco, 1999), pp. 100–103.
28. We caution that the calibration of the ACIS spectral response is still evolving because of the CTI problem (*18*), and spectral fitting for extended structures is likely to improve beyond the work presented here.
29. L. Townsley *et al.*, *Astrophys. J.* **534**, L139 (2000).
30. H. Ebeling, D. A. White, V. N. Rangarajan, *Mon. Not. R. Astron. Soc.*, in press.
31. R. W. O'Connell, J. J. Mangano, *Astrophys. J.* **221**, 62 (1978).
32. P. E. Freeman, V. Kashyap, R. Rosner, D. Q. Lamb, in preparation.
33. H. Kaneda *et al.*, *Astrophys. J.* **491**, 638 (1997).
34. S. Satyapal *et al.*, *Astrophys. J.* **483**, 148 (1997).
35. Z. P. Huang, T. X. Thuan, R. A. Chevalier, J. J. Condon, Q. F. Yin, *Astrophys. J.* **424**, 114 (1994).
36. R. de Grijs, R. W. O'Connell, G. D. Becker, R. A. Chevalier, J. S. Gallagher III, *Astron. J.* **119**, 68 (2000).

37. We express our appreciation for the many scientists and engineers who brought Chandra to fruition, in particular those at the Massachusetts Institute of Technology, Penn State University, and Lockheed Martin who contributed to the ACIS instrument. This research was funded by NASA contract NAS8-38252 to Penn State University.

27 July 2000; accepted 10 October 2000

Defect-Induced Phase Separation in Dipolar Fluids

T. Tlusty* and S. A. Safran*

A defect-induced, critical phase separation in dipolar fluids is predicted, which replaces the usual liquid-gas transition that is driven by the isotropic aggregation of particles and is absent in dipolar fluids due to strong chaining. The coexisting phases are a dilute gas of chain ends that coexists with a high-density liquid of chain branching points. Our model provides a unified explanation for the branched structures, the unusually low critical temperature and density, and the consequent two-phase coexistence "islands" that were recently observed in experiment and simulation.

The critical liquid-gas phase transition (LGT) is a generic feature of simple fluids. When the temperature is decreased below the critical temperature, the simple fluid phase separates into a low-density gas that coexists with a high-density liquid. The phase separation is well understood as the consequence of a temperature-dependent interplay between the entropy loss due to hard-core repulsion and a short-range isotropic attraction, as was first formulated by van der Waals in his equation of state. In contrast, the basic thermodynamics of dipolar fluids, where the attraction is due to long-range anisotropic dipolar forces, are still obscure, including the basic question of whether the LGT exists at all.

Dipolar fluids have numerous scientific and industrial applications, mostly related to the strong field-responsive properties of colloidal ferrofluids (*1*) or electro-rheological fluids (*2*). For these applications, it is crucial to know whether the system exists in a single homogenous phase. Dipolar fluids also have theoretical significance as a fundamental model of statistical mechanics, perhaps the simplest example of an anisotropic fluid, which may provide physical insight for polar fluids such as hydrogen fluoride or even water.

The mean dipolar interaction between two particles is attractive (with a Boltz-

Department of Materials and Interfaces, Weizmann Institute of Science, Rehovot, Israel.

*To whom correspondence should be addressed. E-mail: cptsvi@weizmann.ac.il (T.T.); sam.safran@weizmann.ac.il